remote sensing

MDPI

Article

Mapping Irrigated and Rainfed Wheat Areas Using Multi-Temporal Satellite Data

Ning Jin [1,2,3], Bo Tao [4], Wei Ren [4], Meichen Feng [5], Rui Sun [1], Liang He [6], Wei Zhuang [1] and Qiang Yu [7,*]

1 Key Laboratory of Water Cycle and Related Land Surface Processes, Institute of Geographic Sciences and Natural Resources Research, Beijing 100101, China; j.n.--0613@163.com (N.J.); sunrui11@126.com (R.S.); zhuangw.12b@igsnrr.ac.cn (W.Z.)
2 University of Chinese Academy of Sciences, Beijing 100049, China
3 Shanxi Climate Center, Taiyuan 030002, China
4 Department of Plant and Soil Sciences, College of Agriculture, Food and Environment, University of Kentucky, KY 40506, USA; bo.tao@uky.edu (B.T.); wei.ren@uky.edu (W.R.)
5 Institute of Dry Farming Engineering, Shanxi Agricultural University, Shanxi Taigu 030801, China; fmc101@163.com
6 National Meteorological Center, Beijing 100081, China; xhl860728@163.com
7 School of Life Sciences, University of Technology Sydney, P.O. Box 123, Broadway NSW 2007, Australia
* Correspondence: Qiang.Yu@uts.edu.au; Tel.: +61-2-9514-4142

Academic Editors: Clement Atzberger and Prasad S. Thenkabail
Received: 27 September 2015; Accepted: 29 January 2016; Published: 3 March 2016

Abstract: Irrigation is crucial to agriculture in arid and semi-arid areas and significantly contributes to crop development, food diversity and the sustainability of agro-ecosystems. For a specific crop, the separation of its irrigated and rainfed areas is difficult, because their phenology is similar and therefore less distinguishable, especially when there are phenology shifts due to various factors, such as elevation and latitude. In this study, we present a simple, but robust method to map irrigated and rainfed wheat areas in a semi-arid region of China. We used the Normalized Difference Vegetation Index (NDVI) at a 30 × 30 m spatial resolution derived from the Chinese HJ-1A/B (HuanJing(HJ) means environment in Chinese) satellite to create a time series spanning the whole growth period of wheat from September 2010 to July 2011. The maximum NDVI and time-integrated NDVI (TIN) that usually exhibit significant differences between irrigated and rainfed wheat were selected to establish a classification model using a support vector machine (SVM) algorithm. The overall accuracy of the Google-Earth testing samples was 96.0%, indicating that the classification results are accurate. The estimated irrigated-to-rainfed ratio was 4.4:5.6, close to the estimates provided by the agricultural sector in Shanxi Province. Our results illustrate that the SVM classification model can effectively avoid empirical thresholds in supervised classification and realistically capture the magnitude and spatial patterns of rainfed and irrigated wheat areas. The approach in this study can be applied to map irrigated/rainfed areas in other regions when field observational data are available.

Keywords: irrigated and rainfed areas; growth characteristics; phenology; support vector machines

1. Introduction

Irrigation plays a key role in increasing crop production [1], especially in arid and semi-arid regions. It has been shown that the amount of water used for agricultural irrigation accounts for 84% of total human water consumption [2]. Approximately 40% of the world's harvest is produced on irrigated arable land, which accounts for about 20% of the total arable land area [3], 70% of which is located in Asia [4]. Crop yields are usually higher when crops are fully irrigated as compared to

non-irrigated crops that usually suffer water deficiencies [5]. In China, irrigated land occupies more than 40% of total farmland, but produces 80% of the nation's food [3]. More than two-thirds of all water use in China is from the agriculture sector. It is a widespread concern that China will face serious water shortages as its economy booms and urbanization increases. Realistic estimations of irrigation area are important for evaluating regional water and carbon cycles and ensuring food security [6–10].

Currently, three major methods are used to classify irrigated and rainfed areas. (1) The water resources inventory, developed by the Food and Agriculture Organization of the United Nations (FAO), has been used to map the worldwide distribution of irrigated areas using statistical data [11,12]. Generally, inventory data cannot accurately and timely reflect the spatial distribution of irrigated and rainfed areas. Statistical data are usually based on county/regional information (or even coarser scales) and span different time intervals. Recently, the FAO released a 2010 land cover map of Afghanistan, derived from the Satellite Pour l'Observation de la Terre (SPOT), Landsat imagery and aerial photographs [13]; (2) Unsupervised classification has been widely used for the classification of irrigated and rainfed areas [14,15]. The U.S. Geological Survey (USGS) and International Water Management Institute (IWMI) classified and mapped global irrigated and rainfed areas in the U.S. Geological Survey Global Land Cover Characterization (GLCC) and Global Irrigated Area Map (GIMA), respectively [16–18]. This method can be easily used when local information is sparse; however, it is hard to control the number of classes. In addition, the calibration and combination of each cover type after unsupervised classification is strongly affected by subjective factors; (3) Supervised classification was used by Ozdogan and Gutman (2008) [19] to map irrigated and rainfed areas in the U.S. with a decision tree method based on eight-day synthesis Moderate Resolution Imaging Spectrometer (MODIS) Greenness Index data (500 × 500 m resolution). Kamthonkiat *et al.* (2005) [20] classified irrigated and rainfed rice in Thailand using 10-day synthesis SPOT NDVI data at a 1 × 1 km resolution, 10-day synthesis precipitation data and ancillary data. The advantage of the supervised classification method is that training samples can be controlled; therefore, unnecessary classes can be avoided, though classification accuracy is usually significantly influenced by training samples.

Since the 1980s, satellite remote sensing has been widely used for the classification of irrigated areas because it can provide a near real-time capability to dynamically monitor land surfaces on a regional scale. However, improvements in classification methods for the identification of irrigated areas are still necessary [21]. Currently, the most commonly-used satellite data are MODIS products, with a mean spatial resolution of 250 × 250 m. Such data are generally sufficient to characterize large-scale spatial patterns, but may bring large uncertainties in arid and semi-arid regions, where irrigation is typically practiced in small and scattered areas. Pervez *et al.* (2014) [22] used the same growth period to calculate the time-integrated NDVI (TIN) for irrigated and rainfed wheat. However, there are distinct differences between irrigated and rainfed wheat in growth processes, the length of the growing season and the periods of peak NDVI. Moreover, the NDVI threshold used in the supervised classification method usually has to be modified for local conditions, which may reduce the accuracy of the classification [5,9].

To overcome the aforementioned disadvantages in mapping irrigated and rainfed areas, we propose an improved classification method based on the following three aspects. First, we used data from two of China's small environmental satellites, the HJ-1A/B (HuanJing(HJ) means environment in Chinese) satellites, launched on 6 September 2008. A spatial resolution of 30 × 30 m and a two-day repeat cycle make them suitable for dynamic monitoring of irrigated and rainfed areas on a regional scale [23]. Second, the support vector machine (SVM) algorithm was used as a classification method to avoid subjectivity in the definition of NDVI thresholds. The SVM is a pattern recognition method developed on the basis of statistical learning theory with high flexibility, global optimization, high efficiency and robustness [24–26]. It has been widely used in the remote sensing classification [27–29]. Third, considering the differences between irrigated and rainfed wheat, peak NDVI and TIN were selected as feature vectors for classification. During this process, sowing and maturity dates derived from NDVI thresholds were set as the start and end points of the growing period for TIN calculations.

In this study, we mapped irrigated and rainfed land in the semi-arid hilly areas of Shanxi Province, China. Due to the high fragmentation of arable land, smallholder management, long growth period of winter wheat and dispersed irrigation times, it is difficult to estimate irrigated areas in this region. Until now, there are no reliable maps of irrigated winter wheat in Shanxi Province. Our major research objectives were to: (1) develop a novel classification method for irrigated and rainfed areas based on high resolution satellite data, the SVM algorithm, and site-level observations; (2) map irrigated and rainfed winter wheat in the south central part of Shanxi Province; and (3) quantify the spatial patterns of sowing and maturation dates of winter wheat under different water supply conditions.

2. Study Area

Shanxi Province, located on the central Loess Plateau of Northern China, is characterized by typical loess hills and gully topography (Figure 1). The surface area of Shanxi Province is 156,700 km^2, and approximately 80.1% of the land area is covered with mountains and hills. As the largest coal-producing province, Shanxi Province accounts for one fourth of the total coal production in China [30]. Groundwater is exploited for food production, as well as for coal mining. The climate in most areas of Shanxi Province is semi-arid and is under the influence of the continental monsoon, with obvious zonal and vertical variations. The annual average temperature varies between −1 °C and 14 °C, decreasing from south to north and from plain to mountain areas. The annual average precipitation varies from 400 mm in the northwest to 650 mm in the southeast. Approximately 70% to 80% of the annual precipitation occurs during the monsoon season from June to September.

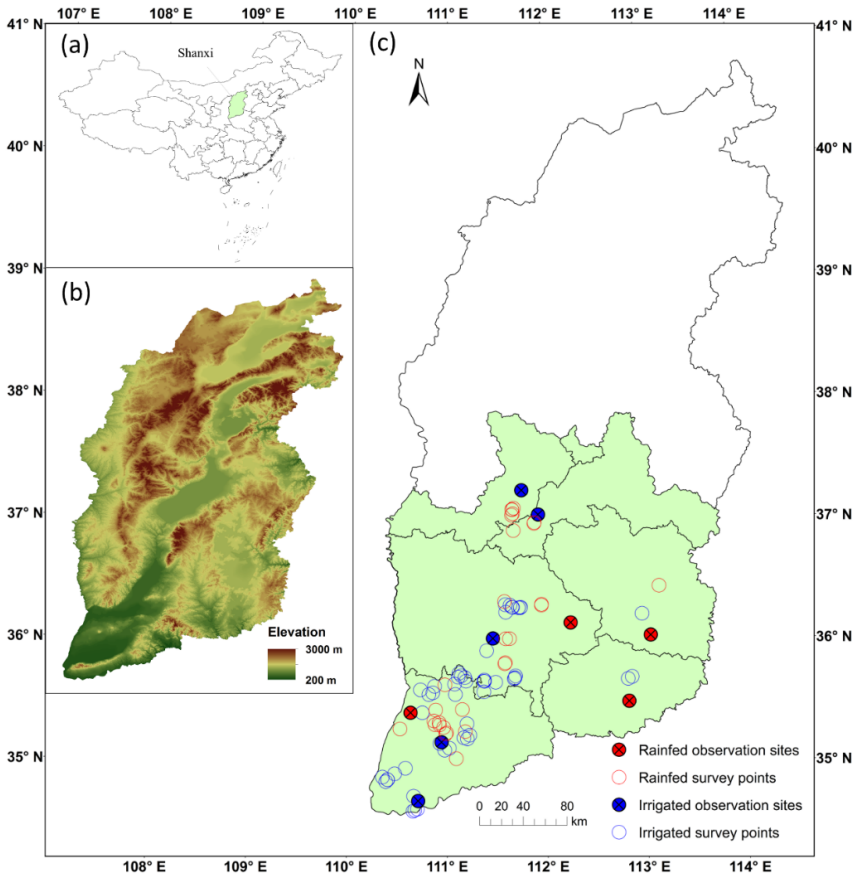

Figure 1. Location of Shanxi Province (**a**); digital elevation map (**b**) and spatial distribution of irrigated and rainfed observation sites and survey points (**c**) across the study area. The irrigated and rainfed observation sites represent agrometeorological stations, while the survey points represent random selected ground survey points.

In the study area, crop cultivation is vulnerable to drought due to little precipitation during critical growth stages. Smallholders comprise a large force in Shanxi's agricultural sector, and the most commonly planted crops include wheat, corn, millet, beans and tubers. Wheat is the most widely-grown staple crop throughout south central Shanxi; it is usually sown during mid-September to late October and harvested from mid-May to early July. The wheat-planting area in south central Shanxi Province was about 710,100 ha during 2010 to 2011. In general, irrigated areas are distributed throughout south central Shanxi. Irrigation activities mainly occur before dormancy, greening, jointing and grain filling, and irrigation is largely determined by the availability of surface and groundwater.

Irrigated areas can be divided into the area equipped for irrigation and the actual irrigated area. The irrigated area is typically smaller than the area equipped for irrigation due to water availability, climatic conditions, economic factors, labor availability, land management decisions, *etc.* In this study, we focus on the actual irrigated area, which reflects the real irrigation conditions.

3. Materials and Methods

3.1. Datasets

3.1.1. Observation Data from Agrometeorological Stations

There are nine agrometeorological stations in south central Shanxi Province that observe wheat growth, five of which observe irrigated wheat. Crop growth, development and yield are strongly influenced by climatic factors, such as temperature, precipitation and solar radiation [31–33]. The water demand of winter wheat during the growing season is approximately between 450.0 and 650.0 mm. The observed precipitation at the agrometeorological stations varies from 83.3 to 190.8 mm during the winter wheat growing period (2011) (Table 1). This amount usually does not meet the water demand of wheat for normal growth, and it is necessary to irrigate crops with supplementary water to reduce water stress at critical growth stages [34]. Generally, irrigated wheat suffers less from water stress compared to rainfed wheat, resulting in distinct differences in growth characteristics.

In this study, we focus on the wheat growth period from 2010 to 2011. During this period, winter wheat suffered from more severe drought stress than during other years. The precipitation throughout the growing season was 48.8 mm lower than the average precipitation during 2006 to 2014. Field survey data show that growth conditions and yield production between irrigated and rainfed wheat are significantly different. The average yield of irrigated wheat is 2.3-times higher than that of rainfed wheat, based on the agrometeorological station observations.

3.1.2. HJ Satellite Data

The HJ satellite (Small Satellite Constellation for Environmental Prediction and Disaster Monitoring) carries two sensors, HJ-1A and HJ-1B, and features two main characteristics, *i.e.*, a short revisit time of two days and large spatial coverage. The swath width of the charged coupled device sensor (CCD) aboard the HJ satellite is 360 km, and the spatial resolution is 30 × 30 meters. The CCD sensor has four bands (blue, green, red and near-infrared) with a spectral range of 0.43 to 0.90 μm and a radiometric resolution of 8 bits. Landsat TM/ETM+ imagery has the same spatial resolution, but has difficulty meeting the high frequency demand for its 16-day return cycle and cloudiness. The MODIS imagery has high temporal resolution, but its spatial resolution is relatively coarse for small and scattered agricultural fields. The HJ satellite has the advantages of both Landsat and MODIS and therefore is more suitable for dynamic monitoring of multi-temporal and spatial variations in irrigated areas.

Table 1. Observed environmental conditions and wheat yield at agrometeorological stations in south central Shanxi Province.

		Yanhu	**Yaodu**	**Ruicheng**	**Wanrong**	**Jincheng**	**Fenyang**	**Jiexiu**	**Anze**	**Changzhi**	**Average**
Irrigated/rainfed		Irrigated	Irrigated	Irrigated	Rainfed	Rainfed	Irrigated	Irrigated	Rainfed	Rainfed	
Elevation (m)		376.0	450.0	507.0	590.0	744.0	749.0	750.0	858.0	991.0	
Longitude		111.02	111.50	110.71	110.83	112.83	111.76	111.93	112.25	113.06	
Latitude		35.03	36.06	34.70	35.40	35.51	37.25	37.05	36.16	36.05	
Sowing dates		10/7	9/28	10/17	9/25	9/21	10/6	10/16	9/30	9/23	9/30
Maturity dates		6/6	6/6	6/12	6/12	6/13	6/26	6/22	6/24	6/20	6/15
Yield (kg/ha)	2011	3825.0	3750.0	4800.0	1935.0	2658.0	5325.0	6150.0	1950.0	3670.5	3784.5
	2006 to 2014	3700.5	5394.0	5286.0	2142.0	3000.0	5674.5	5617.5	2484.0	3621.0	4102.5
Cumulated precipitation (mm)	2011	125.8	102.0	108.0	112.2	118.3	83.3	99.9	190.8	176.5	124.1
	2006 to 2014	162.4	143.9	160.0	194.9	192.0	132.1	127.9	231.2	211.6	172.9
Cumulated temperature (°C)	2011	2258.4	2291.7	2027.7	2520.1	2264.9	2220.5	2055.7	1888.6	2068.5	2177.3
	2006 to 2014	2290.5	2309.1	2039.8	2412.3	2178.8	2224.0	2120.7	1910.7	2032.6	2168.7
Cumulated sunshine duration (hours)	2011	1438.7	1679.1	1481.8	1665.9	1905.8	1513.1	1642.9	1835.2	1845.1	1667.5
	2006 to 2014	1270.1	1317.9	1372.4	1432.6	1665.3	1522.4	1450.8	1654.6	1725.3	1490.2

The HJ satellite datasets span the time period September 2010 to July 2011, covering the whole growth period of wheat (Table 2). Most of the HJ-1 A/B images used in this study are cloud-free. The DN value was converted to radiance values using radiometric calibration coefficients from the China Center for Resources Satellite Data and Application (available at http://www.cresda.com). The images were then processed with ENVI FLAASH for atmospheric correction. Landsat TM8 images (Level: L1T) covering Shanxi Province were used for geometric correction with an error of less than one pixel. When using the FLAASH module, the center position, access time and other information are obtained from the header file of each image. We selected the mode rural aerosol and the atmospheric mode as mid-latitude winter or mid-latitude summer, depending on the acquisition time. NDVI (NDVI = (ρnir − ρred)/(ρnir + ρred)) is calculated from red and near-infrared reflectance. Finally, images of 24 phases were stacked in sequence to produce NDVI time series with a 30 × 30 m spatial resolution.

Table 2. Landsat 8 and HJ-1A/B images used in this study.

Sensor	Year	Date of Imagery
HJ-1A/B CCD	2010	9/11, 9/17, 9/27, 10/5, 10/15, 11/3, 11/13, 11/19, 11/28, 12/8, 12/16, 12/26
	2011	1/12, 1/24, 2/23, 3/10, 3/24, 4/9, 4/24, 5/12, 5/28, 6/7, 6/28, 7/8
Landsat 8	2013	11/18, 11/27, 12/11

3.2. Methods

The major steps involved in mapping irrigated and rainfed wheat areas include the extraction of winter wheat areas, estimation of seeding and maturity dates and the determination of kernel functions and parameters used in the SVM algorithm (Figure 2). The ground information included the latitude, longitude and water management practices (irrigated or rainfed) for the survey sites, which is an essential part during the establishment of SVM classification model. As the corresponding maximum NDVI and TIN can be extracted based on the information of latitude and longitude, the SVM classification model can be established considering the water management conditions (irrigated or rainfed).

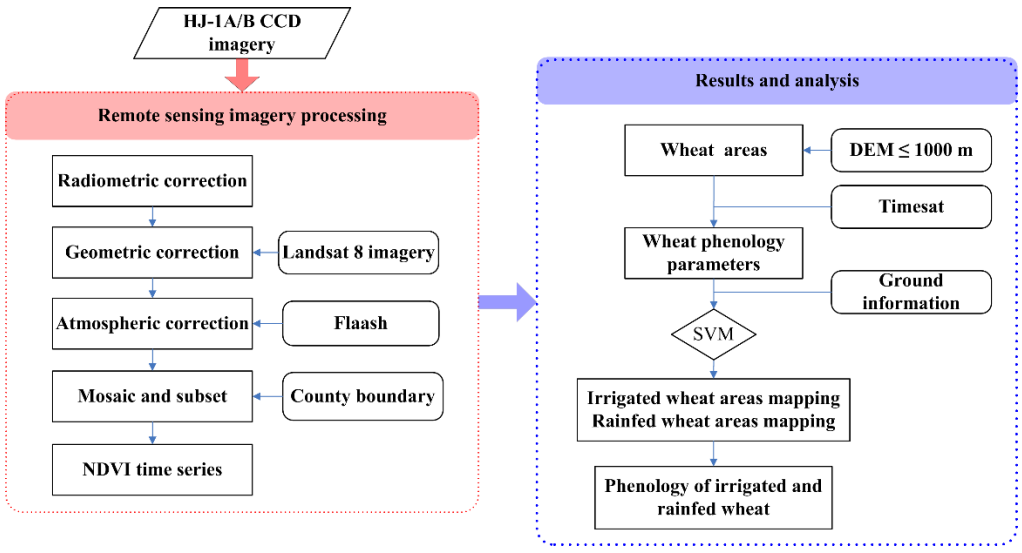

Figure 2. Flowchart of irrigated and rainfed wheat classification.

3.2.1. Wheat Surface Area Extraction

Identifying crop surface area is the first step to mapping irrigated and rainfed areas based on remote sensing images. NDVI time series are commonly used for the classification of different crops, as time series are generally able to represent seasonal rhythms and phenological variations in crops [35–37].

During the growth period of winter wheat, NDVI increases from seeding to dormancy. It then decreases from dormancy to greening, increases again during greening and heading and finally decreases from heading to maturity (Figure 3). For the winter wheat, NDVI exhibits a distinct changing pattern during two periods. The first is from early October to the dormancy period. For other land-use types, NDVI gradually decreases with decreasing temperature. Wheat NDVI, however, gradually increases and reaches a peak in greenness as a result of vigorous growth after sowing. During this period, the time-NDVI slope of wheat is greater than zero, but the corresponding slopes of other land cover types are less than zero. The second occurs from May to June (heading to maturity), which usually corresponds to the late growth period of wheat. Nutrients are gradually transferred from organs, such as roots, stems and leaves, to grains, resulting in a gradual decrease in greenness and NDVI. During this period, the time-NDVI slope of wheat is less than zero, but the slopes for other land-cover types are greater than zero. Therefore, winter wheat can be classified based on the slopes during these two stages.

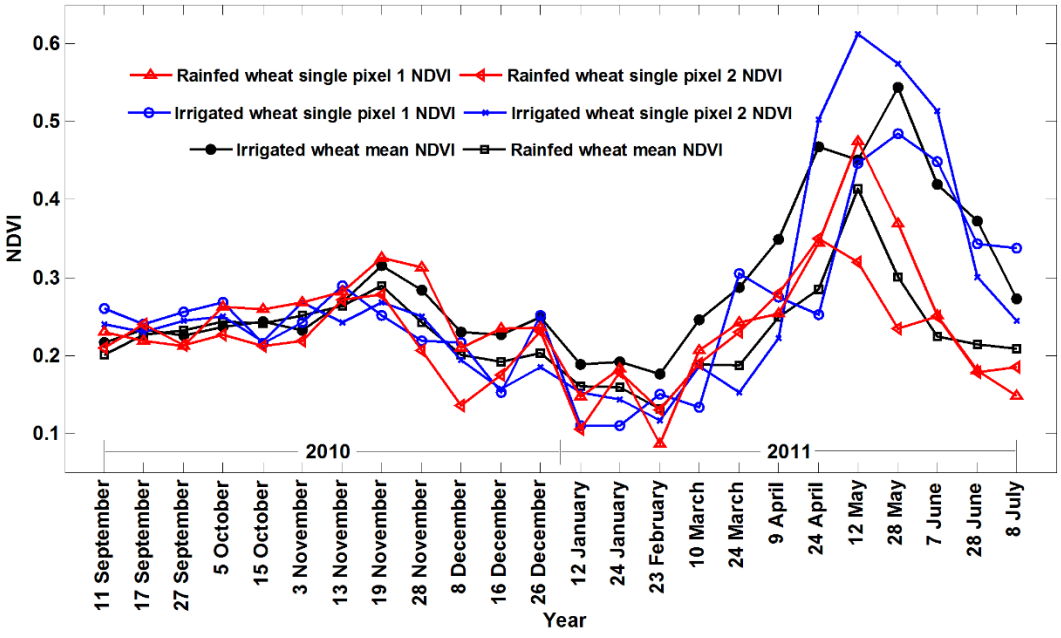

Figure 3. NDVI temporal variations for major land cover types in the south central Shanxi Province.

Generally, the peak NDVI for irrigated wheat is larger than that for rainfed wheat. However, sometimes, the peak NDVI for rainfed wheat may be nearly almost the same as irrigated wheat, or even lightly higher. After rainfed wheat reaches its peak NDVI, the NDVI value decreases rapidly. On the contrary, the peak NDVI for the irrigated wheat appears later and decreases more slowly compared to rainfed wheat.

In this study, we used DEM (digital elevation model) information to extract the wheat surface area. The information of wheat planted areas at the county level was derived from the Shanxi Bureau of Statistics. The relationship between planted areas and their corresponding elevations showed that the elevation of most counties where wheat is planted is generally below 1000 m. Therefore, we defined a 1000-m height as the upper elevation limit for wheat. This means that elevations above 1000 m are not considered suitable for growing wheat.

3.2.2. Estimation of the Wheat Growing Period Based on Satellite Data

In situ observations cannot capture large-scale spatiotemporal changes in phenology. Remote sensing enables low-cost monitoring of vegetative multi-temporal dynamics over the entire region and therefore is a powerful tool to examine phenological changes on a regional scale [38,39].

NDVI represents seasonal and annual variations in crop growth and development (*i.e.*, cyclical changes from planting, emergence, heading to maturity and harvest). Estimation of plant phenology using NDVI time series has been widely carried out during recent decades [40–43]. Many phenological parameters can be derived from remote sensing time series data, such as average NDVI, maximum NDVI, TIN (the integrated NDVI from sowing to maturity, defined as the area of the region between the fitted function and the zero level [44]), date of maximum NDVI and length of the growing season. The classification accuracy of remote sensing imagery can be improved by combining these phenological parameters.

NDVI time series reflecting vegetation growth processes are usually continuous and smooth curves. During the acquisition process, however, satellite data are subject to various interferences, such as solar and observation angles, clouds, water vapor and aerosols, resulting in fluctuations in time series and changes in seasonal trends, which may affect the estimation of vegetation phenology. Therefore, it is necessary to smooth time series of original vegetation index data to reduce noise. In this study, double logistic functions were used to smooth the raw NDVI time series [44–46].

Usually, the start of vegetation growth derived from satellite remote sensing is later than the time of the first leaf unfolding or budburst [47]. It does not represent the beginning of the growing season when individual leaves turn green, but when canopy greenness reaches a specific value that can be recognized by a satellite sensor. Earlier studies have used dynamic threshold methods to estimate the start and end of the growing season for natural vegetation based on NDVI time series data [43,48,49]. However, for cropland, there is usually a period after crop sowing when crops cannot be recognized with remote sensing, which means that the sowing date cannot be directly detected. Lobell *et al.* (2013) [50] defined the green-up date as the earliest time at which vegetation growth can be reliably detected with satellite sensors. They found that the date should be offset from the actual sowing date by a fixed number of days. They compared satellite-based sowing dates and ground-based observations in Punjab and found that the average difference between these dates is two days, indicating that satellite remote sensing is capable of realistically estimating the sowing date of wheat.

In this study, double logistic functions were fit to each NDVI time series on a pixel-by-pixel basis to estimate green-up and maturity dates using Timesat [44]. Then, the wheat sowing date was obtained based on the relationship between the green-up and sowing dates presented by Lobell *et al.* (2013) [50].

3.2.3. NDVI Time Series-Based Classification

Relationship between the NDVI time series and vegetation activities has been well established theoretically and empirically. The NDVI curve properties and characteristics can generate a set of metrics (such as the onset of greening/senescence, timing of maximum NDVI, the growing season length, rates of NDVI changes, *etc.*) that measure the timing and magnitude of NDVI response and summarize the spatial and temporal distribution of crop growth and phenology, therefore being widely used as an input for classification. A range of classification algorithms has been developed based on NDVI time series, such as the supervised classification methods, spectral matching techniques, decision tree algorithms, neural network methods, support vector machines, and so on [21,22,51–53].

3.2.4. Classification Features Selection: Peak NDVI and Time-Integrated NDVI

The growth characteristics (growth conditions, growth period and yield) between irrigated and rainfed wheat are significantly different, which can be reflected by dynamic changes in NDVI time series. First, the peak of NDVI for irrigated wheat is larger than that for rainfed wheat [54,55]. Maximum NDVI for a yearly time series is a proxy for the peak level of photosynthetic activity, maximum biomass and the densest vegetation cover [5]. Second, the time at which rainfed wheat reaches its maximum NDVI is earlier than that for irrigated wheat, because rainfed wheat generally suffers from severer water stress, resulting in accelerated growth. Therefore, peak NDVI and TIN values during the wheat growth period can be used as feature vectors to classify irrigated and rainfed wheat.

3.2.5. Classification of SVM

SVM is a pattern recognition method that can solve pattern recognition problems, such as small sample size, nonlinearity, high dimensionality and local minima [24]. SVM has been widely used in remote sensing studies and can improve classification accuracy as compared to traditional classification methods, such as the maximum likelihood classification [27,56,57]. SVM projects raw input data into a higher dimensional space to enlarge the separability between different classes when they cannot be appropriately separated by a linear hyperplane. This transformation is realized through different kernel functions and training samples, which cause more scatter after projection into a higher dimensional space. Linear, polynomial, radial basis (RBF) and sigmoidal functions are the most commonly-used core functions, and the performance of the classification model is strongly influenced by different kernel functions [58].

(1) Maximum Margin Hyperplane

The maximum margin hyperplane is the farthest hyperplane from the training samples. The smallest distance from each training sample to a given hyperplane is regarded as a margin. The maximum margin hyperplane is related to the classification hyperplane that the margin between different classes is the largest [26]. The training samples that define the maximum margin hyperplane make up the support vector, and the other training samples do not contribute to the estimation of the hyperplane position. Accordingly, it is possible to obtain high classification accuracy through SVM using a small number of samples.

(2) Variable Determination

Variable determination plays a key role in improving the predictive ability of trained SVMs and ensuring that unknown data can be accurately predicted. The performance of SVMs is mainly influenced by kernel functions. Once the type of kernel functions is selected, variables (such as γ) and the error penalty C, which are closely related to the kernel function, should be carefully chosen to ensure the most satisfactory classification results. A large value of C corresponds to higher error (*i.e.*, overfitting the training sample), which can reduce the generalization capacity. It has been suggested that SVMs show a high degree of robustness to variations in variable values [59].

Variables (such as γ and C) related to kernels can be estimated through a grid search, which is similar to an exhaustive search within a solution space [60]. The performance of a t-fold cross-validation is evaluated by including randomly-generated variables into the classifier. Then, the values of these variables are tuned and the performance is re-evaluated until all of the selected variables are tested. The variable pair (γ and C) that exhibits the highest cross-validation accuracy is selected.

(3) *t*-Fold Cross-Validation

During the process of *t*-fold cross-validation, training samples are equally divided into a user-defined number of subsets, *t*. When establishing a SVM classification model, one of the *t* subsets is set as a validation sample, and the remaining *t*-1 subsets are set as training samples. This process is repeated sequentially until all datasets have been tested. The average error of a *t*-trial cross-validation is defined as the classification error. The percentage of correctly classified validation samples is defined as the accuracy. This method can effectively avoid overfitting and less learning, thus resulting in more realistic and accurate classification results compared with the one-trial method.

4. Results

4.1. Planted Wheat Area and Growth Periods Derived from Satellite Remote Sensing in South Central Shanxi Province

The estimated wheat-planting area in south central Shanxi Province was 774,538 ha during 2010 to 2011, slightly higher than that determined by the census data (710,100 ha). This estimated area was then used as a basis for the subsequent classification of irrigated and rainfed wheat.

Nine sowing and maturity dates were estimated with HJ-1A/B satellite data, corresponding to the nine agrometeorological stations, respectively (Table 3). The differences between the estimated results (sowing and maturity dates) and ground-based observations were within 12 days, less than 13.5 days of the average revisit interval of HJ-1A/B imagery, indicating that the estimation accuracy of the wheat growth period is acceptable. The estimations at Jiexiu and Ruicheng stations exhibited larger errors due to the small wheat plots, and hence, the associated mixing of wheat pixels with those of other land use types. The average differences in sowing and maturity dates between HJ-1A/B and ground-based estimates were within six and two days respectively, indicating that the method used in this study is robust for estimating the wheat growing period.

Table 3. Comparison of sowing and maturity dates (DOY) estimated with HJ-1A/B satellite and ground-based data.

	Reported Sowing Date	HJ Sowing Date	Difference (HJ-Reported)	Reported Maturity Date	HJ Maturity Date	Difference (HJ-Reported)
Yanhu	280	270	−10	157	164	7
Yaodu	271	267	−4	157	165	8
Ruicheng	290	275	−15	163	170	7
Wanrong	268	269	1	163	169	6
Jincheng	264	267	3	164	170	6
Fenyang	279	271	−8	177	172	−5
Jiexiu	289	271	−18	173	170	−3
Anze	273	268	−5	175	172	−3
Changzhi	266	268	2	171	173	2
Average	276	270	−6	167	169	2

4.2. Spatial Distribution of Wheat Sowing and Maturity Dates in South Central Shanxi Province

Our results show that, in 2010, wheat sowing in south central Shanxi Province mainly occurred during 17 September and 10 October (Figure 4a). The sowing dates significantly varied with increasing elevation ($y = -0.0106x + 271.1763$, $p < 0.05$). In 2011, the wheat maturity phase mainly occurred from 2 June to 29 June. Lagged maturity dates significantly varied with increasing elevation ($y = 0.0101x + 162.0040$, $p < 0.05$) (Figure 4b). The spatial distributions of sowing and maturity dates generally exhibited opposite patterns, *i.e.*, sowing occurred earlier and harvest occurred later at high elevation, whereas at low elevation, sowing occurred later and harvest earlier. In general, the spatial

patterns of sowing and maturity dates were related with elevation and latitude, suggesting that temperature is a key variable controlling this spatial pattern.

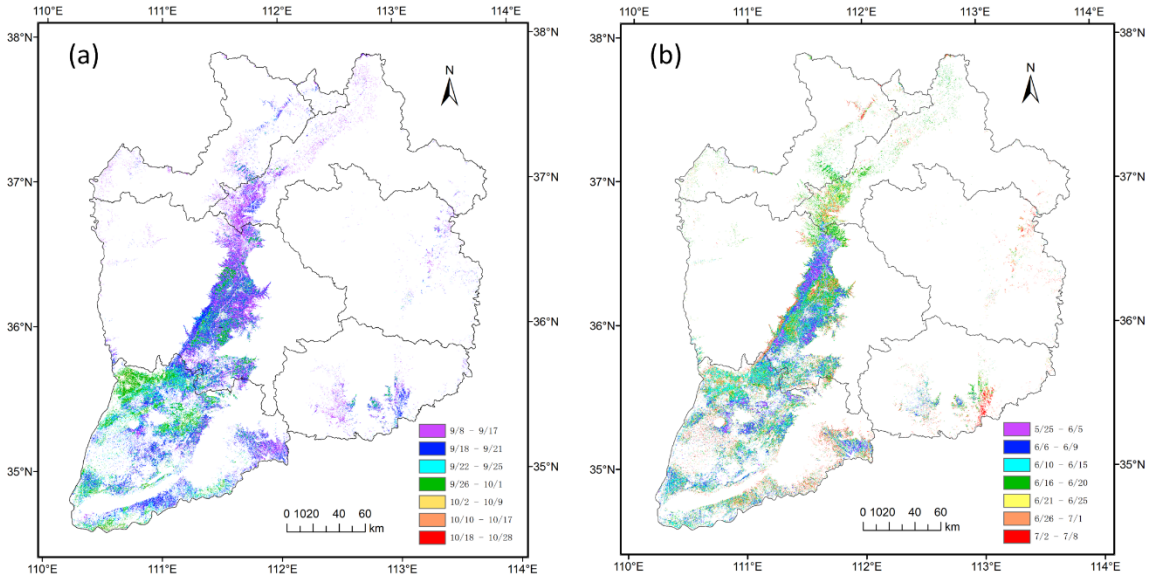

Figure 4. Spatial patterns of wheat sowing (**a**) and maturity (**b**) dates in south central Shanxi Province.

4.3. Validation of the SVM Classification Model

Peak NDVI and TIN of 83 irrigated and rainfed wheat survey samples were used as feature vectors during classification. The variables C and γ in SVM were estimated through a five-fold cross-validation using a grid search (Figure 5). Then, based on this pair of global optimal parameters (C = 1.4142 and γ = 2.8284), the SVM model was used for the classification of irrigated and rainfed wheat in south central Shanxi Province.

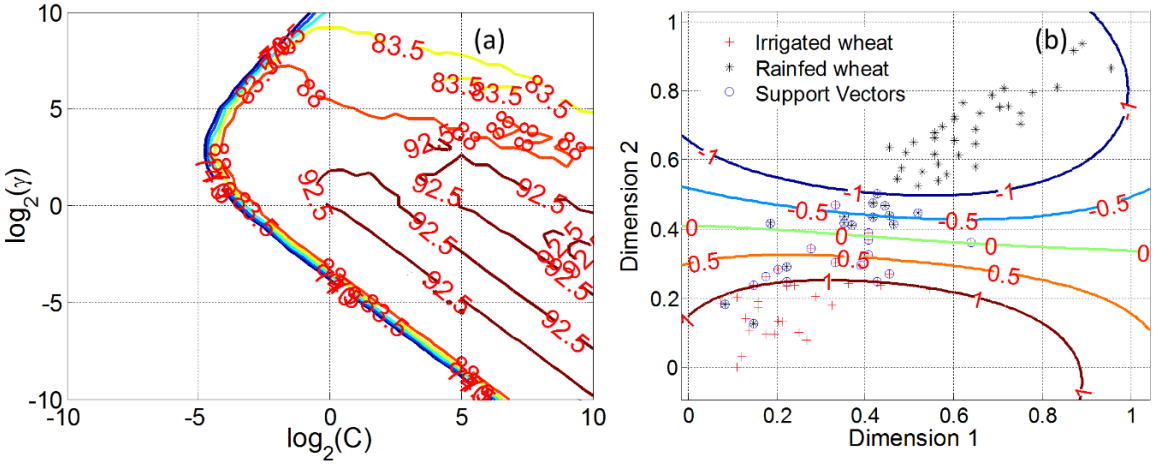

Figure 5. SVM parameter selection (**a**) and accuracy of five-fold cross-validation (**b**) for training samples. (**a**) shows the pair of global optimal parameters (C and γ) through the grid search; (**b**) is the visualization of classification of irrigated and rainfed wheat when the training data were mapped into a higher dimensional feature space using the RBF kernel function.

An additional 774 testing samples (388 irrigated and 386 rainfed wheat) were randomly selected from Google-Earth and used to validate the capacity of the SVM model. The overall accuracy was 92.4% for the NDVI time series-based classification model, while the overall accuracy was 96.0% for the peak NDVI and TIN classification model (Table 4). It is inevitable to use the same start and end period for the NDVI time series in the NDVI time series-based method. Therefore, discrepancies in the growing period (sowing and maturity dates) and growing length of irrigated and rainfed wheat are greatly ignored. This may cause uncertainty in the classification results, especially in arid and semi-arid regions, such as south central Shanxi Province in this study. The peak NDVI and TIN values can reflect crop growth characteristics under different water conditions. Thus, the use of peak NDVI and TIN as feature vectors for classification has a large advantage over the NDVI time series-based method and may result in higher classification accuracy.

Table 4. Error matrix for SVM classification. TIN, time-integrated.

Data Sources	**Google Earth Additional Testing Samples**							
Feature vectors	NDVI time series				Peak NDVI and TIN			
Classification	Irrigated	Rainfed	Total	User's accuracy (%)	Irrigated	Rainfed	Total	User's accuracy (%)
Irrigated	**349**	20	369	94.6	**377**	20	397	95.0
Rainfed	39	**366**	405	90.4	11	**366**	377	97.1
Total	388	386	774		388	386	774	
Producer's accuracy (%)	89.9	94.8			97.2	94.8		
Overall accuracy (%)	92.4				96.0			

4.4. Spatial Distribution of Irrigated and Rainfed Wheat in South Central Shanxi Province

The spatial distribution of irrigated and rainfed wheat was scattered and staggered in most regions of south central Shanxi Province. This pattern is primarily due to the high fragmentation in wheat fields, which is different from the continuous distribution of wheat in plains (Figure 6). Furthermore, topography and water resources also influence irrigation activities.

In this study, the classification results derived from satellite imagery were quantitatively evaluated against the ground reference information. First, we evaluated the ratio of irrigated-to-rainfed wheat area. The Second Agricultural Census of Shanxi Province provides the areas of irrigated and rainfed arable land, but does not distinguish different crop types. Moreover, these census datasets were manually collected, and only the available water resources and irrigation facilities were considered, which are not equivalent to the actual irrigated area. In this case, the ratio of irrigated-to-rainfed wheat area was used to verify the accuracy of the SVM classification result. According to census data from agricultural sectors in Shanxi Province, the ratio of irrigated-to-rainfed wheat area was approximately 4:6, whereas our result was 4.4:5.6. Second, our classification results of irrigated and rainfed wheat in the survey sites agreed with the ground-based photographs taken from 26 to 31 May 2011. The survey photos showed that irrigated wheat is stout with dark green leaves, whereas rainfed wheat is shorter with yellow leaves and significantly slower in growth. Third, the regional spatial distribution of irrigated and rainfed wheat from this study is consistent with a visual interpretation of high spatial resolution Google Earth images, which reflect wheat growth conditions (Figure 6a,b). The discrepancies between irrigated and rainfed wheat are mainly due to water availability.

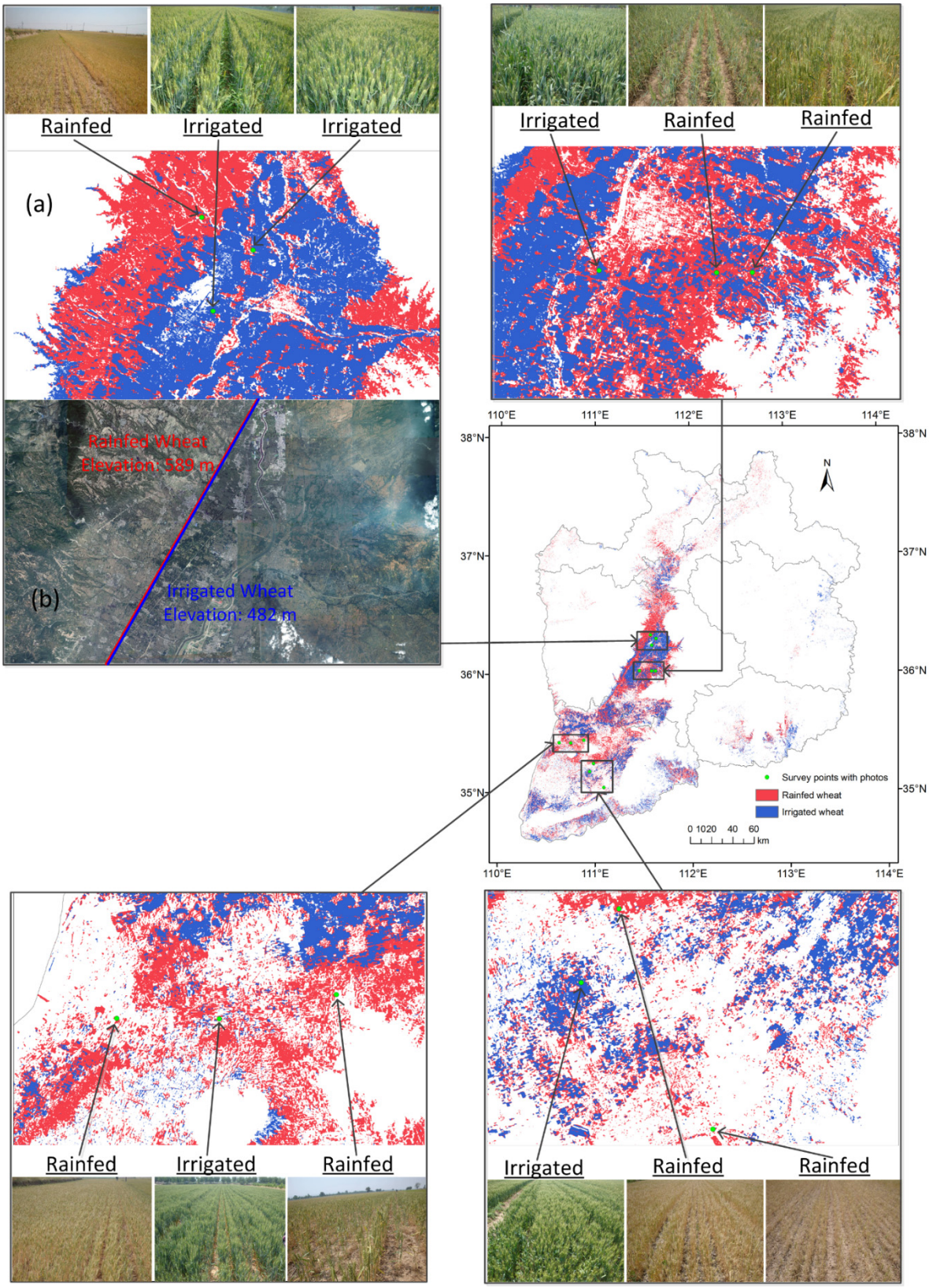

Figure 6. Spatial distribution of irrigated and rainfed wheat in south central Shanxi Province. (**a**) is the classification of irrigated and rainfed areas for a region that containing three survey sites; (**b**) is the Google Earth image of the same region that corresponding to (**a**).

Google Earth multi-spectral imagery provides topography and land cover/land use information. Water availability is influenced by topography and thus results in different wheat growth conditions. These discrepancies were clearly reflected through visual interpretation of Google Earth imagery (Figure 6b). The growth conditions of wheat planted in the majority of the northwest region were worse due to scarce water resources compared to wheat planted in the southeast.

Irrigated wheat generally benefits from better growth conditions and a longer growth period compared to the rainfed wheat and, hence, has higher NDVI and TIN values (Figure 7). The spatial distribution patterns of peak NDVI and TIN agree well with the distribution of irrigated and rainfed wheat.

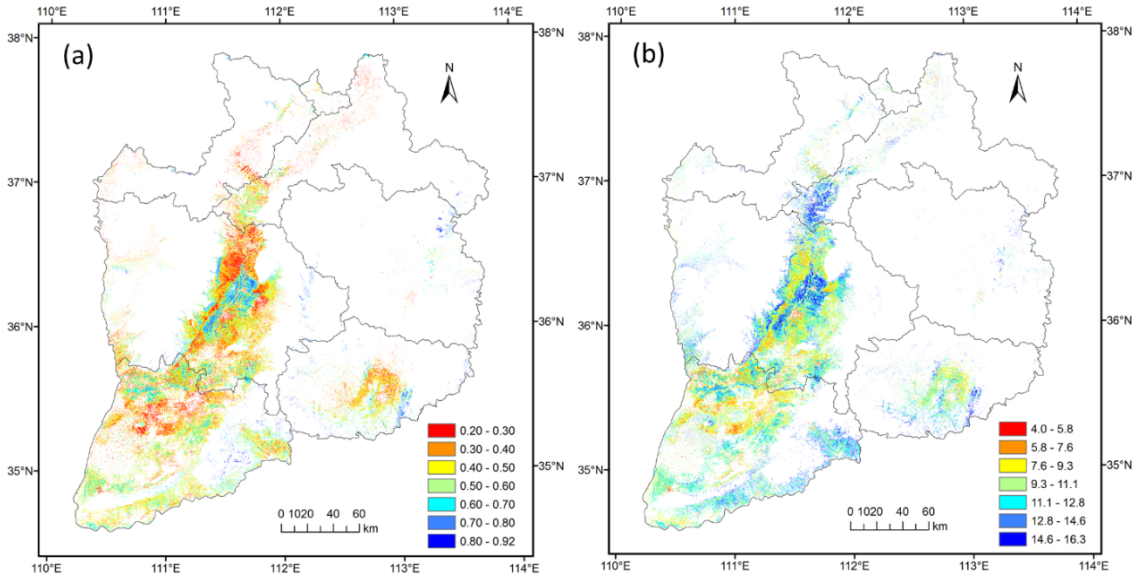

Figure 7. Spatial distribution of maximum NDVI (**a**) and TIN (**b**) of wheat in south central Shanxi Province.

4.5. Spatial Distribution of Sowing and Maturity Dates of Irrigated and Rainfed Wheat in South Central Shanxi Province

Spatial variations in sowing and maturity dates are associated with various factors, such as water conditions (*i.e.*, irrigated or rainfed conditions), latitude and elevation [61,62]. The sowing dates of rainfed and irrigated wheat in south central Shanxi Province were mainly between 17 September and 10 October 2010 (Figure 8a,b). Rainfed and irrigated wheat exhibited similar spatial patterns with respect to sowing dates, increasing from southwest to northeast and were significantly related to elevation (rainfed: $y = -0.0082x + 269.4273$; irrigated: $y = -0.0124x + 272.6023$; $p < 0.05$). The maturity dates of rainfed wheat were mainly from 2 to 21 June, whereas irrigated wheat matured between 8 and 29 June (Figure 8c,d). Rainfed and irrigated wheat exhibited different spatial patterns with respect to maturity, and the overall maturity dates of irrigated wheat was 15 days later than that of rainfed wheat. The maturity dates of rainfed and irrigated wheat were significantly related to elevation (rainfed: $y = 0.0077x + 160.6768$; irrigated: $y = 0.0197x + 160.0829$; $p < 0.05$), increasing from southwest to northeast, and irrigated wheat varied faster than rainfed wheat.

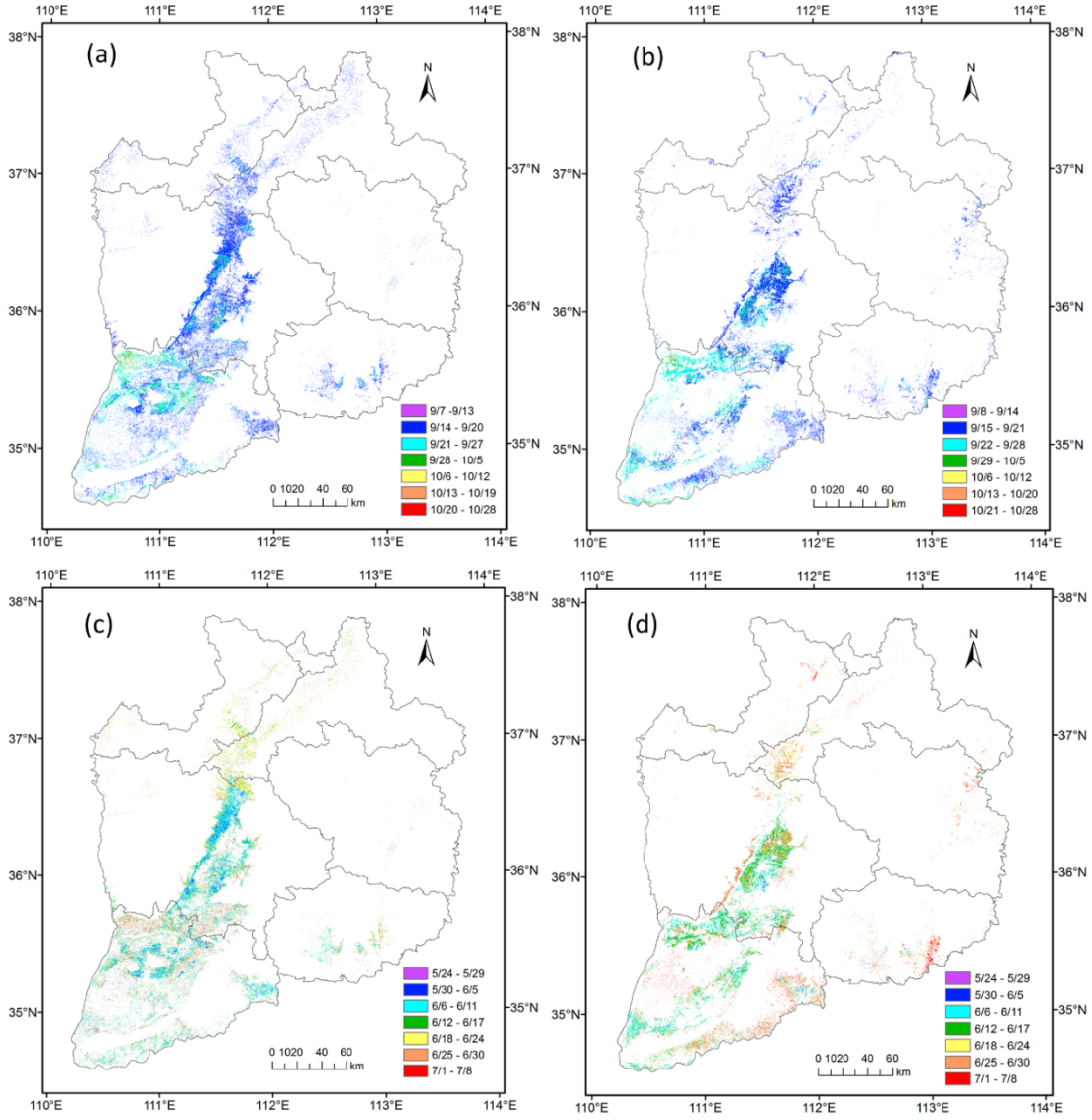

Figure 8. Sowing dates of rainfed (**a**) and irrigated (**b**) wheat. Maturity dates of rainfed (**c**) and irrigated (**d**) wheat in south central Shanxi Province.

5. Discussion

5.1. Validation of SVM Classification Model

Water availability is the main limiting factor for crop growth in arid and semi-arid regions. There are large discrepancies between irrigated and rainfed wheat in Shanxi Province. Compared to irrigated wheat, rainfed wheat matures earlier and experiences inferior growth conditions. The peak NDVI and TIN values extracted from remote sensing data can realistically reflect these discrepancies. Therefore, these two feature vectors were used to establish an SVM classification model for irrigated and rainfed wheat. Quality and quantitative evaluations were conducted to validate the SVM classification model. The results showed that our proposed peak NDVI and TIN-based method has obvious advantages and obtains higher classification accuracy as compared to conventional NDVI time series-based methods.

5.2. Spatial Distribution and Variation Patterns of Wheat Sowing and Maturity Dates

The growth period and crop yield are strongly influenced by water deficit. Rainfed wheat may suffer severe water stress and exhibit significant differences compared to irrigated wheat. During

the growing season, an increase in air temperature may result in a shorter growth period and earlier maturity date under deficient water supply, as shown in rainfed wheat in arid and semi-arid areas in this study. The growth and crop yield of rainfed wheat are severely affected by water deficit, e.g., during the filling stage of winter wheat when photosynthetic products in roots, stems and other organs are transported to grains.

This study quantified spatial variations and rates changes of the wheat growth period under different water supply conditions based on an enhanced classification method. The results show that the sowing dates of rainfed and irrigated wheat exhibit similar spatial patterns, and both are significantly related to elevation. Irrigated wheat varies faster than rainfed wheat. The maturity dates of rainfed and irrigated wheat are significantly postponed when elevation increases; however, they exhibit distinct spatial patterns.

5.3. Uncertainties and Future Needs

Uncertainties are inherent for most satellite data, including the HJ-1A/B satellite. Errors may exist when translating satellite data into sowing and maturity dates. In this study, a 30 × 30 m pixel was considered as 100% irrigated or rainfed, and thus, fragmented small fields may not have been well resolved. The above two aspects may have induced uncertainty in our estimated irrigated and rainfed surface areas. Typically, satellite data with higher spatial resolution perform better in mapping irrigated and rainfed areas for regions with small and scattered crop fields, but such data may be limited by a long satellite revisit time. Satellite data, such as MODIS, have a high temporal resolution and provide broad coverage area. Therefore, data assimilation is required to take advantage of different satellites and obtain high spatiotemporal resolution datasets for irrigated area mapping. Heterogeneous and small patchy crop areas are another challenge for classification. Some methods (e.g., mixed pixel decomposition) are needed to estimate the fraction of irrigated and rainfed areas in one grid cell, especially for regions with scattered farmland and a variable topographic surface.

6. Conclusions

A simple, but effective method based on an SVM algorithm was developed to map irrigated and rainfed wheat areas in a semi-arid region of China. This method avoids repeated tuning of thresholds in supervised classification. The overall accuracy of the Google-Earth testing samples is 96.0%, indicating that the SVM classification model is robust. The estimated ratio of irrigated-to-rainfed wheat area in this study is close to that estimated by the agricultural sector of Shanxi Province. The classification of irrigated and rainfed areas for the survey points also agrees with the field level photographs. In addition, maps of maturity dates and sowing dates were generated. It was shown that irrigated and rainfed wheat exhibit distinct maturity dates, although the spatial patterns of sowing dates are similar.

Accurate training samples, which were obtained from ground surveys in this study, are essential for the presented method. The proposed method can be applied in other arid and semi-arid regions with the availability of accurate training samples and multi-temporal data at high spatial and temporal resolutions similar to HJ-1 A/B (or higher). The HJ-1 A/B has an advantage over Landsat in temporal resolution, although they have the same spatial resolution in the red and near-infrared band. Different temporal resolution may influence the classification result of irrigated and rainfed wheat area, and the comparison of HJ-1 A/B time series with Landsat or Sentinel time series for classifications in partially-irrigated areas is a potential field area of future research. In addition, the performance of the proposed method in areas with more than one major crop type needs to be evaluated in the future.

Acknowledgments: The present research was funded by the National Natural Science Foundation of China (Grant Nos. 41171086, 41371119).

Author Contributions: Ning Jin was the main author of the manuscript. Bo Tao, Wei Ren and Qiang Yu revised the manuscript. Meichen Feng provided some ground reference information. Rui Sun, Liang He and Wei Zhuang provided some valuable suggestions. All of the authors have read and approved the final manuscript.

Conflicts of Interest: The authors declare no conflict of interest.

References

1. Grogan, D.S.; Zhang, F.; Prusevich, A.; Lammers, R.B.; Wisser, D.; Glidden, S.; Li, C.; Frolking, S. Quantifying the link between crop production and mined groundwater irrigation in China. *Sci. Total Environ.* **2015**, *511*, 161–175. [CrossRef] [PubMed]
2. Shiklomanov, I.A. Appraisal and assessment of world water resources. *Water Int.* **2000**, *25*, 11–32. [CrossRef]
3. Du, T.; Kang, S.; Sun, J.; Zhang, X.; Zhang, J. An improved water use efficiency of cereals under temporal and spatial deficit irrigation in north China. *Agric. Water Manag.* **2010**, *97*, 66–74. [CrossRef]
4. Boucher, O.; Myhre, G.; Myhre, A. Direct human influence of irrigation on atmospheric water vapour and climate. *Clim. Dyn.* **2004**, *22*, 597–603. [CrossRef]
5. Pervez, M.S.; Brown, J.F. Mapping irrigated lands at 250-m scale by merging modis data and national agricultural statistics. *Remote Sens.* **2010**, *2*, 2388–2412. [CrossRef]
6. Gordon, L.J.; Steffen, W.; Jönsson, B.F.; Folke, C.; Falkenmark, M.; Johannessen, Å. Human modification of global water vapor flows from the land surface. *Proc. Natl. Acad. Sci. USA* **2005**, *102*, 7612–7617. [CrossRef] [PubMed]
7. Li, J.; Inanaga, S.; Li, Z.; Eneji, A.E. Optimizing irrigation scheduling for winter wheat in the north china plain. *Agric. Water Manag.* **2005**, *76*, 8–23. [CrossRef]
8. Vörösmarty, C.J.; Douglas, E.M.; Green, P.A.; Revenga, C. Geospatial indicators of emerging water stress: An application to africa. *AMBIO: A J. Hum. Environ.* **2005**, *34*, 230–236. [CrossRef]
9. Ozdogan, M.; Salvucci, G.D.; Anderson, B.T. Examination of the bouchet-morton complementary relationship using a mesoscale climate model and observations under a progressive irrigation scenario. *J. Hydrometeorol.* **2006**, *7*, 235–251. [CrossRef]
10. Wu, Y.; Jia, Z.; Ren, X.; Zhang, Y.; Chen, X.; Bing, H.; Zhang, P. Effects of ridge and furrow rainwater harvesting system combined with irrigation on improving water use efficiency of maize (*Zea mays* L.) in semi-humid area of China. *Agric. Water Manag.* **2015**, *158*, 1–9. [CrossRef]
11. Döll, P.; Siebert, S. A digital global map of irrigated areas. *ICID J.* **2000**, *49*, 55–66.
12. Siebert, S.; Döll, P.; Hoogeveen, J.; Faures, J.-M.; Frenken, K.; Feick, S. Development and validation of the global map of irrigation areas. *Hydrol. Earth Syst. Sci. Discuss.* **2005**, *2*, 1299–1327. [CrossRef]
13. Food and Agriculture Organization of the United Nations. *Provincial Land Cover Atlas of Islamic Republic of Afghanistan*; FAO: Rome, Italy, 2010.
14. Droogers, P. *Global Irrigated Area Mapping: Overview and Recommendations*; IWMI: Colombo, Sri Lanka, 2002; Volume 36.
15. Biggs, T.; Thenkabail, P.; Gumma, M.; Scott, C.; Parthasaradhi, G.; Turral, H. Irrigated area mapping in heterogeneous landscapes with MODIS time series, ground truth and census data, Krishna Basin, India. *Int. J. Remote Sens.* **2006**, *27*, 4245–4266. [CrossRef]
16. Loveland, T.; Reed, B.; Brown, J.; Ohlen, D.; Zhu, Z.; Yang, L.; Merchant, J. Development of a global land cover characteristics database and igbp discover from 1 km avhrr data. *Int. J. Remote Sens.* **2000**, *21*, 1303–1330. [CrossRef]
17. Thenkabail, P.S. *An Irrigated Area Map of the World (1999), Derived from Remote Sensing*; IWMI: Colombo, Sri Lanka, 2006; Volume 105.
18. Thenkabail, P.S.; Biradar, C.M.; Noojipady, P.; Dheeravath, V.; Li, Y.; Velpuri, M.; Gumma, M.; Gangalakunta, O.R.P.; Turral, H.; Cai, X. Global irrigated area map (GIAM), derived from remote sensing, for the end of the last millennium. *Int. J. Remote Sens.* **2009**, *30*, 3679–3733. [CrossRef]
19. Ozdogan, M.; Gutman, G. A new methodology to map irrigated areas using multi-temporal MODIS and ancillary data: An application example in the continental us. *Remote Sens. Environ.* **2008**, *112*, 3520–3537. [CrossRef]
20. Kamthonkiat, D.; Honda, K.; Turral, H.; Tripathi, N.; Wuwongse, V. Discrimination of irrigated and rainfed rice in a tropical agricultural system using SPOT vegetation NDVI and rainfall data. *Int. J. Remote Sens.* **2005**, *26*, 2527–2547. [CrossRef]
21. Zheng, B.; Myint, S.W.; Thenkabail, P.S.; Aggarwal, R.M. A support vector machine to identify irrigated crop types using time-series landsat NDVI data. *Int. J. Appl. Earth Obs. Geoinf.* **2015**, *34*, 103–112. [CrossRef]
22. Pervez, M.S.; Budde, M.; Rowland, J. Mapping irrigated areas in afghanistan over the past decade using MODIS NDVI. *Remote Sens. Environ.* **2014**, *149*, 155–165. [CrossRef]

23. Lu, S.; Wu, B.; Yan, N.; Wang, H. Water body mapping method with HJ-1A/B satellite imagery. *Int. J. Appl. Earth Obs. Geoinf.* **2011**, *13*, 428–434. [CrossRef]
24. Vapnik, V.N. *Statistical Learning Theory*; Wiley: New York, NY, USA, 1998; Volume 1.
25. Ben-Hur, A.; Weston, J. A user's guide to support vector machines. In *Data Mining Techniques for the Life Sciences*; Springer: New York, NY, USA, 2010; pp. 223–239.
26. James, G.; Witten, D.; Hastie, T.; Tibshirani, R. *An Introduction to Statistical Learning*; Springer: New York, NY, USA, 2013.
27. Foody, G.M.; Mathur, A. The use of small training sets containing mixed pixels for accurate hard image classification: Training on mixed spectral responses for classification by a SVM. *Remote Sens. Environ.* **2006**, *103*, 179–189. [CrossRef]
28. Alcantara, C.; Kuemmerle, T.; Prishchepov, A.V.; Radeloff, V.C. Mapping abandoned agriculture with multi-temporal MODIS satellite data. *Remote Sens. Environ.* **2012**, *124*, 334–347. [CrossRef]
29. Barrett, B.; Nitze, I.; Green, S.; Cawkwell, F. Assessment of multi-temporal, multi-sensor radar and ancillary spatial data for grasslands monitoring in ireland using machine learning approaches. *Remote Sens. Environ.* **2014**, *152*, 109–124. [CrossRef]
30. Aunan, K.; Fang, J.; Vennemo, H.; Oye, K.; Seip, H.M. Co-benefits of climate policy—Lessons learned from a study in Shanxi, China. *Energy Policy* **2004**, *32*, 567–581. [CrossRef]
31. Tao, F.; Zhang, Z.; Xiao, D.; Zhang, S.; Rötter, R.P.; Shi, W.; Liu, Y.; Wang, M.; Liu, F.; Zhang, H. Responses of wheat growth and yield to climate change in different climate zones of China, 1981–2009. *Agric. For. Meteorol.* **2014**, *189*, 91–104. [CrossRef]
32. Yu, Q.; Li, L.; Luo, Q.; Eamus, D.; Xu, S.; Chen, C.; Wang, E.; Liu, J.; Nielsen, D.C. Year patterns of climate impact on wheat yields. *Int. J. Climatol.* **2014**, *34*, 518–528. [CrossRef]
33. Rao, B.B.; Chowdary, P.S.; Sandeep, V.; Pramod, V.; Rao, V. Spatial analysis of the sensitivity of wheat yields to temperature in India. *Agric. For. Meteorol.* **2015**, *200*, 192–202. [CrossRef]
34. Wanjura, D.; Hatfield, J.; Upchurch, D. Crop water stress index relationships with crop productivity. *Irrig. Sci.* **1990**, *11*, 93–99. [CrossRef]
35. Lobell, D.B.; Asner, G.P. Cropland distributions from temporal unmixing of MODIS data. *Remote Sens. Environ.* **2004**, *93*, 412–422. [CrossRef]
36. Galford, G.L.; Mustard, J.F.; Melillo, J.; Gendrin, A.; Cerri, C.C.; Cerri, C.E. Wavelet analysis of MODIS time series to detect expansion and intensification of row-crop agriculture in Brazil. *Remote Sens. Environ.* **2008**, *112*, 576–587. [CrossRef]
37. Liu, M.W.; Ozdogan, M.; Zhu, X. Crop type classification by simultaneous use of satellite images of different resolutions. *IEEE Trans. Geosci. Remote Sens.* **2014**, *52*, 3637–3649. [CrossRef]
38. Cong, N.; Wang, T.; Nan, H.; Ma, Y.; Wang, X.; Myneni, R.B.; Piao, S. Changes in satellite—Derived spring vegetation green—Up date and its linkage to climate in China from 1982 to 2010: A multimethod analysis. *Glob. Change Biol.* **2013**, *19*, 881–891. [CrossRef] [PubMed]
39. You, X.; Meng, J.; Zhang, M.; Dong, T. Remote sensing based detection of crop phenology for agricultural zones in china using a new threshold method. *Remote Sens.* **2013**, *5*, 3190. [CrossRef]
40. White, M.A.; BEURS, D.; Kirsten, M.; DIDAN, K.; INOUYE, D.W.; RICHARDSON, A.D.; JENSEN, O.P.; O'KEEFE, J.; ZHANG, G.; NEMANI, R.R. Intercomparison, interpretation, and assessment of spring phenology in north america estimated from remote sensing for 1982–2006. *Glob. Chang. Biol.* **2009**, *15*, 2335–2359. [CrossRef]
41. Busetto, L.; Colombo, R.; Migliavacca, M.; Cremonese, E.; Meroni, M.; Galvagno, M.; Rossini, M.; Siniscalco, C.; Morra Di Cella, U.; Pari, E. Remote sensing of larch phenological cycle and analysis of relationships with climate in the alpine region. *Glob. Change Biol.* **2010**, *16*, 2504–2517. [CrossRef]
42. JEONG, S.J.; HO, C.H.; GIM, H.J.; Brown, M.E. Phenology shifts at start *vs.* End of growing season in temperate vegetation over the northern hemisphere for the period 1982–2008. *Glob. Change Biol.* **2011**, *17*, 2385–2399. [CrossRef]
43. Jeganathan, C.; Dash, J.; Atkinson, P. Remotely sensed trends in the phenology of northern high latitude terrestrial vegetation, controlling for land cover change and vegetation type. *Remote Sens. Environ.* **2014**, *143*, 154–170. [CrossRef]
44. Jönsson, P.; Eklundh, L. Timesat—A program for analyzing time-series of satellite sensor data. *Comput. Geosci.* **2004**, *30*, 833–845. [CrossRef]

45. Atkinson, P.M.; Jeganathan, C.; Dash, J.; Atzberger, C. Inter-comparison of four models for smoothing satellite sensor time-series data to estimate vegetation phenology. *Remote Sens. Environ.* **2012**, *123*, 400–417. [CrossRef]
46. Butt, B.; Turner, M.D.; Singh, A.; Brottem, L. Use of MODIS NDVI to evaluate changing latitudinal gradients of rangeland phenology in Sudano-Sahelian West Africa. *Remote Sens. Environ.* **2011**, *115*, 3367–3376. [CrossRef]
47. White, M.A.; Thornton, P.E.; Running, S.W. A continental phenology model for monitoring vegetation responses to interannual climatic variability. *Glob. Biogeochem. Cycles* **1997**, *11*, 217–234. [CrossRef]
48. Kross, A.; Fernandes, R.; Seaquist, J.; Beaubien, E. The effect of the temporal resolution of NDVI data on season onset dates and trends across Canadian broadleaf forests. *Remote Sens. Environ.* **2011**, *115*, 1564–1575. [CrossRef]
49. Cong, N.; Piao, S.; Chen, A.; Wang, X.; Lin, X.; Chen, S.; Han, S.; Zhou, G.; Zhang, X. Spring vegetation green-up date in China inferred from SPOT NDVI data: A multiple model analysis. *Agric. For. Meteorol.* **2012**, *165*, 104–113. [CrossRef]
50. Lobell, D.B.; Ortiz-Monasterio, J.I.; Sibley, A.M.; Sohu, V. Satellite detection of earlier wheat sowing in India and implications for yield trends. *Agric. Syst.* **2013**, *115*, 137–143. [CrossRef]
51. Thenkabail, P.; GangadharaRao, P.; Biggs, T.; Krishna, M.; Turral, H. Spectral matching techniques to determine historical land-use/land-cover (LULC) and irrigated areas using time-series 0.1-degree AVHRR pathfinder datasets. *Photogramm. Eng. Remote Sens.* **2007**, *73*, 1029–1040.
52. Geerken, R.; Zaitchik, B.; Evans, J.P. Classifying rangeland vegetation type and coverage from NDVI time series using fourier filtered cycle similarity. *Int. J. Remote Sens.* **2005**, *26*, 5535–5554. [CrossRef]
53. Verbeiren, S.; Eerens, H.; Piccard, I.; Bauwens, I.; Van Orshoven, J. Sub-pixel classification of spot-vegetation time series for the assessment of regional crop areas in Belgium. *Int. J. Appl. Earth Obs. Geoinf.* **2008**, *10*, 486–497. [CrossRef]
54. Aparicio, N.; Villegas, D.; Casadesus, J.; Araus, J.L.; Royo, C. Spectral vegetation indices as nondestructive tools for determining durum wheat yield. *Agron. J.* **2000**, *92*, 83–91. [CrossRef]
55. Wardlow, B.D.; Egbert, S.L. Large-area crop mapping using time-series MODIS 250 m NDVI data: An assessment for the U.S. Central Great Plains. *Remote Sens. Environ.* **2008**, *112*, 1096–1116. [CrossRef]
56. Huang, C.; Davis, L.; Townshend, J. An assessment of support vector machines for land cover classification. *Int. J. Remote Sens.* **2002**, *23*, 725–749. [CrossRef]
57. Pal, M. Support vector machine—based feature selection for land cover classification: A case study with DAIS hyperspectral data. *Int. J. Remote Sens.* **2006**, *27*, 2877–2894. [CrossRef]
58. Tso, B.; Mather, P. *Classification Methods for Remotely Sensed Data*; CRC Press: Boca Raton, FL, USA, 2009.
59. Belousov, A.; Verzakov, S.; Von Frese, J. A flexible classification approach with optimal generalisation performance: Support vector machines. *Chemom. Intell. Lab. Syst.* **2002**, *64*, 15–25. [CrossRef]
60. Chang, C.-C.; Lin, C.-J. LibSVM: A library for support vector machines. *ACM Trans. Intell. Syst. Technol.* **2011**, *2*, 27. [CrossRef]
61. Tao, F.; Zhang, S.; Zhang, Z. Spatiotemporal changes of wheat phenology in China under the effects of temperature, day length and cultivar thermal characteristics. *Eur. J. Agron.* **2012**, *43*, 201–212. [CrossRef]
62. Xiao, D.; Tao, F. Contributions of cultivars, management and climate change to winter wheat yield in the North China plain in the past three decades. *Eur. J. Agron.* **2014**, *52*, 112–122. [CrossRef]